Journal of Thermal Analysis and Calorimetry
https://doi.org/10.1007/s10973-023-12177-2

Thermal decomposition of calcium propionate: films and powders

Sihem Zaidi[1,2] · Daniel Sanchez-Rodriguez[1] · Jordi Farjas[1] · Dammak Mohamed[2] · Pere Roura-Grabulosa[1]

Received: 1 November 2022 / Accepted: 9 April 2023

Abstract
The thermal decomposition of calcium propionate, in inert and oxidative atmospheres, has been investigated by thermogravimetry combined with infrared evolved gas analysis; the main volatiles formed during thermal decomposition have been identified. The intermediate and final products have been characterized by infrared spectroscopy, x-ray diffraction, elemental analysis and scanning electron microscopy. The different mechanisms involved in thermal decomposition are discussed as a function of atmosphere and sample structure. The kinetics of the decomposition and the ability of powders to undergo a thermal runaway are also investigated.

Keywords Calcium propionate · Thermal decomposition · TGA-EGA · Food preservatives

Introduction

Calcium propionate $Ca(CH_3CH_2CO_2)_2$ (CaProp) is widely used as chemical preservative [1, 2] and additive [3] in the food, pharmaceutical and paper industries [4] for its antimicrobial properties. CaProp has also been used as a precursor for belite cement clinkers [5]. Besides, CaProp is useful in reducing harmful emissions of sulfur dioxide (SO_2) and nitrogen oxides (NOx) from coal-fired power plants; SO_2 and NOx are captured through their reaction with CaO and the volatiles released during CaProp thermal decomposition, respectively [6]. CaProp decomposes when heated, either during food preparation, production of belite cement clinkers or operation of coal-fired power plants. Therefore, disclosing the different decomposition pathways and the volatiles that evolve during thermal decomposition of CaProp, as well as their dependence on the surrounding atmosphere and sample morphology, is of crucial importance.

Thermal decomposition of carboxylate salts of M(II) and M(III) in inert atmosphere follows a radical path that yields symmetrical ketones [7–12]. Conversely, in the presence of water or oxygen, hydrolysis and oxidation of propionate salts yields propionic acid and acetaldehyde [12, 13]. The latter mechanisms have been reported mainly in samples in the form of films. In contrast, in powder samples, the slow intra-particle transport of oxygen and water [14] results in an almost inert local atmosphere near the particles that hinders hydrolysis and oxidation of the propionate salts [13, 15, 16] thus favoring the radical path.

Several papers have analyzed the thermal decomposition of CaProp by thermogravimetry (TG) and differential thermal analysis (DTA) in dry air and in inert atmospheres [17–22]. It has been observed that, in inert atmosphere, the decomposition is preceded by melting of CaProp around 390°C [17, 20, 21] and that decomposition starts at lower temperature in air [17, 18]. Concerning the volatiles, 3-pentanone has been reported to be the main volatile formed during thermal decomposition in N_2 [21, 22]. However, a comprehensive analysis of volatiles and decomposition mechanism including oxidative and humid atmospheres has not yet been performed.

Although it has been shown that films tend to decompose differently than powders [12–15, 23] and that the analysis of films is useful to reveal the occurrence of a reactive mechanism, so far, the thermal decomposition of CaProp has been studied only in the form of powder. Furthermore, kinetic analysis of CaProp decomposition have yielded inconclusive results. The decomposition in N_2 [21] gave abnormally high activation energies of 315 kJ mol^{-1} whereas in O_2 [24] very large fluctuations of the activation energy (between 83 and 346 kJ mol^{-1}) were reported during the decomposition

✉ Jordi Farjas
jordi.farjas@udg.cat

[1] Physics, Universitat de Girona, Campus Montlivi, Edif. PII, Girona 17003, Catalonia, Spain

[2] Laboratoire de Chimie Inorganique, Faculté des Sciences de Sfax, University of Sfax, BP 1171, Sfax 3000, Tunisia

Published online: 30 April 2023

course. Also the kinetic analysis can be affected by a local overheating. In fact, the distorted evolutions and sample overheating observed in [18] are probably related to the occurrence of a thermal runaway.

In this study, in situ evolved gas analysis (EGA) using Fourier transform infrared spectroscopy (FTIR) is applied to analyze the volatiles formed during the thermal decomposition of CaProp and the effect of the sample morphology (film or powder). It will be shown that, depending on the atmosphere, two mechanisms involving the formation of different volatiles are at work. In addition, we will show how heat transport affects the decomposition kinetics and, in particular, we will state that, during thermal analysis experiments in oxygen, powders can easily undergo a thermal runaway.

Materials and methods

The starting solution was obtained by dissolving calcium propionate (Glentham ≥ 99%) in propionic acid (Merck, ≥ 99%). It was sonicated until complete dissolution of the salt to a concentration $[Ca^{2+}] = 1.5M$. Films were obtained depositing the initial solution on $10 \times 10\ mm^2$ $LaAlO_3$ (LAO) substrates and drying them at 70°C for 5 min. Film thicknesses after decomposition were estimated from the mass of the $CaCO_3$ film after decomposition and assuming that the film density matches that of calcite, ($2.71 g\ cm^{-3}$). The final thickness was about 4.5 µm.

The initial, intermediate and final decomposition products were characterized by FTIR, x-ray diffraction (XRD) and elemental analysis (EA). FTIR analysis was performed with a Bruker ALPHA spectrometer connected to an attenuated total reflectance module. AE was performed with a Perkin Elmer 2400 elemental analyzer with the following detection limits 0,20% for H and 0,72% for C. XRD spectra were obtained with a Bruker AXS D8 ADVANCE diffractometer with a Cu-Kα source (1.5406 Å) operating at 40 kV and 40 mA.

The evolution of volatiles and mass loss during thermal decomposition of films and powders was studied by coupled TG-EGA techniques. Simultaneous thermogravimetric (TG) and differential scanning calorimetry (DSC) analyses were performed on a Mettler Toledo thermobalance, model TGA/DSC1, at 10 °C min^{-1} under a gas flow of 20 mL min^{-1} of high purity N_2 (Air Liquide, ≥ 99.999%) or synthetic air through the protective inlet and 60 mL min^{-1} of high purity N_2 or O_2 through the reactive inlet. Water-saturated gases at the reactive inlet were obtained by bubbling the carrier gas in water at 25 °C and atmospheric pressure. Uncovered Al_2O_3 pans of 350 µL were used. In situ EGA/FTIR was obtained by connecting the TGA gas outlet to an ALPHA Bruker FTIR gas analyzer via a 40 cm long steel tube heated to 200°C. The maximum temperature of the TGA measurements was 600°C.

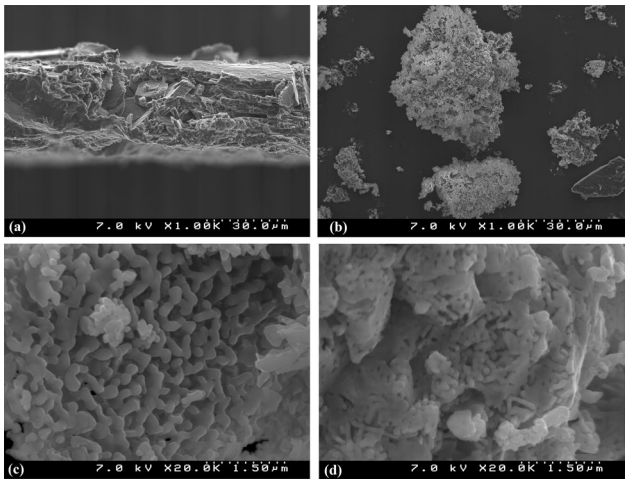

Fig. 1 SEM image showing the cross section of a peeled film (**a**) and powder (**b**) treated at 250°C. Idem for a peeled film (**c**) and powders (**d**) treated at 500°C. All treatments were performed with a heating ramp of 10°C min^{-1} and constant flow of dry O_2

DSC analysis was performed on a Mettler Toledo DSC821e. Samples of about 2 mg were placed inside 40 µL aluminum pans that were covered with a perforated lid to allow gas exchange. DSC measurements were performed under a constant heating rate of 10°C min^{-1} and under a gas flow rate of 40 mL min^{-1} of high purity N_2 or O_2.

Different TG-EGA measurements were performed varying the sample morphology (film or powder) and the atmosphere. Films were decomposed in dry O_2 (**DO**), in humid O_2 (**HO**), in dry N_2 (**DN**), in humid N_2 (**HN**) and in dry air (**A**). Powder samples are labeled with a prime (e.g., powders in dry O2 are identified as **DO'**).

Finally, a ZEISS DSM 960A Scanning Electron Microscope (SEM) was used to observe the morphology of peeled films and powders that were deposited on a conductive tape.

Results and discussion

Characterization of the initial product

The cross section of a peeled film is shown in Fig. 1a. The films are porous: in Fig. 1c, it can be seen that, after CaProp decomposition, the film exhibits a microstructure of characteristic length of 0.15 µm. The aspect of the initial CaProp powder is shown in Fig. 1b. It consists mainly of particles of lengths around 300 µm. Likewise, these particles are highly porous, the characteristic length of the microstructure is around 0.25 µm (not shown). After CaProp decomposition,

the structure is finer with a characteristic length of 0.1 µm (Fig. 1d).

From EA (see Table 1) we can state that there is an excess of carbon and hydrogen in the dried films with respect to the expected values for anhydrous CaProp (%C = 38.7, %H = 5.41). Conversely, the amount of carbon in the initial powders is below the expected one of CaProp. As we will see in Sect. 3.2, the higher amount of carbon and hydrogen in dried films is related to the presence of coordinated propionic acid while the inferior amount of carbon in powders is due to the presence of water of crystallization. In particular, the amount of carbon and hydrogen in films corresponds to 0.5 moles of propionic acid per mole of CaProp (%C = 40.3, %H = 5.87) while, for the initial powder, the EA values are consistent with an amount of 0.3 moles of water per mole of CaProp (%C = 37.3, %H = 5.62).

The XRD spectrum in Fig. 2a of the initial powder evidences the presence of two phases: anhydrous and monohydrated CaProp. Therefore, the powders are partially hydrated, which is consistent with the amount of 0.3 moles of water per mole of CaProp determined from the EA. In contrast, the spectrum of the dry film does not match that of anhydrous or monohydrate CaProp because the presence of propionic acid results in a different crystal structure.

Table 1 Mass percentage of carbon and hydrogen determined from elemental analysis of the initial sample and its product after decomposition at different temperatures. They can be compared with the expected values of CaProp or CaCO3 (inside parentheses). "–": values below detection limits

Compound	C Found (expected) mass%	H Found (expected) mass%
Dry film	39.9 (38.7)	6.03 (5.41)
CaProp powder	37.3 (38.7)	5.62 (5.41)
DO at 250°C	38.5 (38.7)	5.59 (5.41)
DO' at 250°C	38.6 (38.7)	5.18 (5.41)
DO' at 500°C	12.0 (12.0)	– (0)
DN' at 500°C	13.7 (12.0)	– (0)

The IR spectra in Fig. 2b of the dried film and the initial powder agree with the assignments reported for propionate salts in [4, 19, 25]. In addition, the broad band around 3400 cm^{-1} reveals the presence of coordinated water in the initial powder. The most distinctive bands of metal carboxylates are the asymmetric and symmetric absorptions of the COO stretching, $\nu_{as}COO^-$ and $\nu_s COO^-$. The carboxylate bond and the crystalline structure are highly dependent on the presence of water of crystallization [17, 26]. It has been stated that the separation between the asymmetric and symmetric carboxylate bands $\Delta\nu = \left[\nu_{as}(COO^-) - \nu_s(COO^-)\right]$ can be used to determine the type of carboxylate-metal complexation [26, 27]. For example, by comparing with sodium propionate [26, 28], it has been proposed that chelating coordination exists when $\Delta\nu < 134.6\ cm^{-1}$, bridging coordination exists when $\Delta\nu \geq 134.6\ cm^{-1}$ and monodentate coordination appears when $\Delta\nu > 180\ cm^{-1}$. In Fig. 2, we observe that the initial powder presents two asymmetric carboxylic bands at 1541 and 1577 cm^{-1}, which are consistent with the coexistence of two phases: anhydrous and monohydrate CaProp. By comparison with the IR spectra obtained after dehydration at 250 °C, we can assign the absorption at 1577 cm^{-1} to anhydrous CaProp. For the anhydrous CaProp, $\Delta\nu = 162 cm^{-1}$ (a very similar value, $\Delta\nu = 165\ cm^{-1}$, was determined for anhydrous copper propionate [15]) that corresponds to a bridging ligand coordination. Conversely, $\Delta\nu = 125\ cm^{-1}$ for monohydrate CaProp (an identical value was obtained for hydrated yttrium propionate [13]) which can be attributed to a bidentate chelating coordination mixed with a bridging coordination. Finally, only one asymmetric carboxylic band is observed at 1537 cm^{-1} for the films confirming that only one CaProp phase is formed in the films. The presence of coordinated propionic acids also affects the carboxylate-metal complexation; in this case $\Delta\nu = 121\ cm^{-1}$ suggesting a bidentate chelating coordination mixed with some bridging coordination.

Dehydration and removal of propionic acid

The evolution of the sample mass with temperature has been measured by TG for films and powders heated at 10 °C min^{-1} and under different atmospheres. In Fig. 3a, only experiments performed under dry atmosphere are shown because no effect was observed due to the presence of water vapor. The TG curves have been normalized to the mass of the sample at 250 °C because, at this temperature, water and propionic acid have already been removed from the films and powder.

Water and propionic acid evolve at around 110 °C and 167 °C, as revealed by the low temperature steps observed in the TG curves (Fig. 3a), and their associated endothermic DSC peaks (Fig. 3b). In fact, at these temperatures, the only signal detected by EGA-FTIR (insets of Fig. 3) corresponds to these two volatiles. Given that the boiling point of propionic acid (141.2 °C) is well below its evolution temperature (167 °C), we conclude that, in the films, there is some coordination with the salt.

The amount of water (5%) and propionic acid (18–23%) obtained from the TG curves agree with the molar amount deduced from EA, since 0.3 moles of water and 0.5 moles of propionic acid per mole of CaProp correspond to 4.2% and 20% (in mass), respectively. The presence of water in

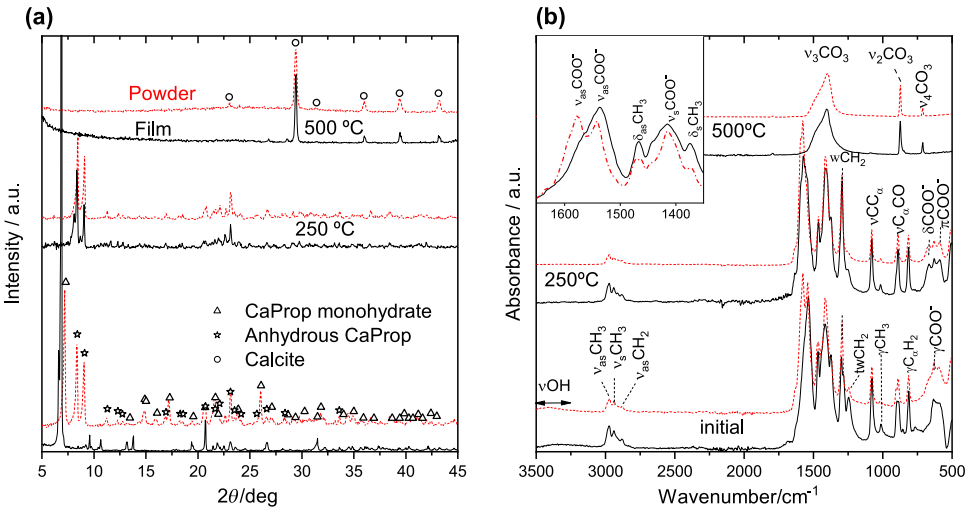

Fig. 2 XRD (**a**) and IR (**b**) spectra of the dried film, initial powder and of the solid residue of films and powders at different temperatures when heated at 10 °C min^{-1} in inert atmosphere. Inset in (**b**): magnification of the initial powder and dried film IR spectra in the range from 1350 to 1650 cm^{-1}. Symbols: reference XRD spectra of anhydrous and monohydrate CaProp [20] and calcite (JCPDS pattern PDF 5-586). Assignment of the infrared peaks: ν stretching; δ bending; γ torsion; w wagging and tw twisting

powder can be attributed to exposure to ambient water vapor. As for films, they contain propionic acid because it has been used as solvent for their preparation (Sect. 2).

Powder decomposition

The thermal stability of pure CaProp depends essentially on the surrounding gas. In inert atmosphere (**DN'**) CaProp is stable up to 385 °C (onset temperature in Fig. 3). At this temperature, a small endothermic peak (Fig. 3b) reveals the melting of CaProp [17, 20, 21]. The coincidence between the melting point and the onset of decomposition seems to indicate that the former triggers the latter. To confirm this aspect, we have performed experiments at different heating rates. In these experiments, at the melting point, it is observed that for a heating rate of 2.5 K min^{-1} 10% of CaProp has already decomposed while for 40 K min^{-1} the decomposition has not yet started. Therefore, CaProp melting does not trigger the decomposition.

In volatile diffusion-controlled processes, melting significantly accelerates the reaction rate. However, in inert atmosphere, we do not observe a significant change in reaction rate at the melting point. In fact, CaProp follows the radical decomposition pathway characteristic of carboxylate [7, 8, 10–12]. This pathway involves the formation of alkyl and acyl radicals from the salt:

$$Ca\left(C_2H_5CO_2\right)_2 \rightarrow C_2H_5CO\cdot + C_2H_5\cdot + CaCO_3. \quad (1)$$

And, in a second stage, the alkyl and acyl radicals combine to form 3-pentanone:

$$C_2H_5CO\cdot + C_2H_5\cdot \rightarrow C_2H_5COC_2H_5. \quad (2)$$

Thus, the radical decomposition of CaProp in an inert atmosphere results in the formation of 3-pentanone and calcium carbonate:

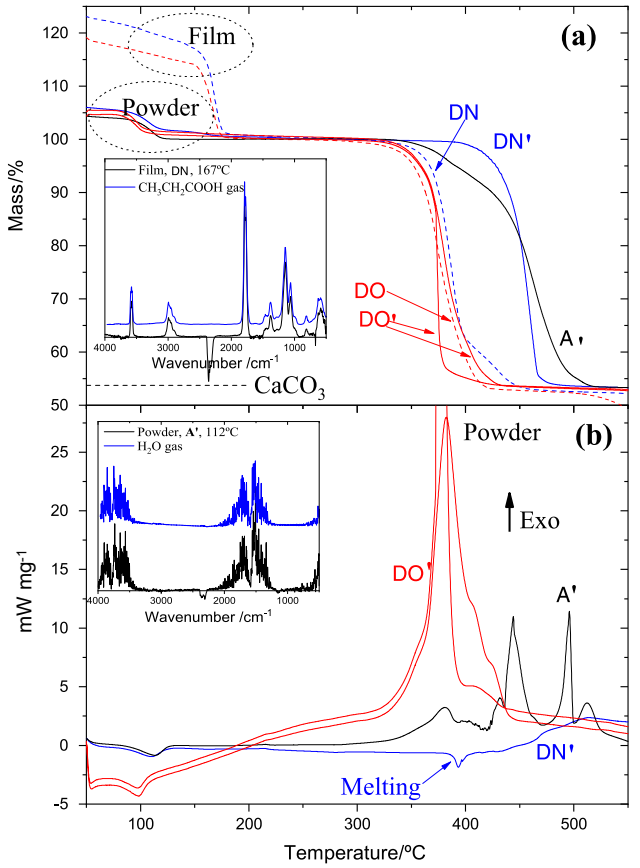

Fig. 3 **a** TG curves showing the influence of atmosphere and sample morphology on the decomposition of CaProp at 10 °C min^{-1} for powders and films. Inset: FTIR spectrum of the volatiles evolved at 167 °C for a film in dry N_2. **b** Corresponding DSC curves for powders. Inset: FTIR spectrum of the volatiles evolved at 112 °C for powders in dry air. Reference FTIR spectra for propionic acid and water have been obtained from [29]

$$Ca\left(C_2H_5CO_2\right)_2 \rightarrow C_2H_5COC_2H_5 + CaCO_3. \quad (3)$$

Simultaneous TG-EGA/FTIR analysis (Fig. 4a) reveals that the 3-pentanone formation rate follows the mass loss rate, −DTG, (DTG is the time derivative of the TG signal). Note that, in the early stages of the decomposition, the DTG signal shows some oscillations (Fig. 4a). These oscillations are the result of gas bubbling in the molten CaProp. The FTIR spectrum of the evolved volatiles at the peak temperature, 459 °C (Fig. 5a), perfectly matches the reference spectrum of 3-pentanone [29] except for a weak absorption at 2340 cm^{-1} that is related to residual CO_2. The absence of CO_2, as expected from reaction 3, confirms that no other reaction competes with the radical decomposition.

Furthermore, the absence of CO_2 indicates that $CaCO_3$ does not decompose to form CaO, in agreement with the XRD and IR results (Fig. 2). The XRD and IR curves of the solid residue at 500 °C show only the characteristic peaks of calcite (IR peaks at 1405, 874 and 712 cm^{-1} [30, 31]).

According to the XRD and FTIR results, the mass of the solid residue at 500 °C is 54.0%, very close to that of $CaCO_3$ formation (53.7%). EA, confirms the presence of carbon in the sample and the complete elimination of hydrogen atoms at 500 °C (Table 1). However, the amount of carbon is slightly higher than expected for $CaCO_3$. Since the final product is not white (as expected for $CaCO_3$), but gray, some carbonaceous residue probably remains at 500 °C. This carbon residue may be related to an alternative radical combination [12]:

$$\begin{aligned} C_2H_5CO\cdot &\rightarrow C_2H_5\cdot + CO \\ 2C_2H_5\cdot &\rightarrow C_4H_{10}. \end{aligned} \quad (4)$$

Subsequently, the disproportionation of carbon monoxide leads to the formation of carbon [32]:

$$2CO \rightarrow C + CO_2. \quad (5)$$

In oxygen, the decomposition of the powders begins well before melting, at about 310 °C. From Fig. 3b it is clear that, in oxygen, the reaction is highly exothermic compared to the inert case. As we will see in Sect. 3.5, this high reaction enthalpy makes the decomposition kinetics highly dependent on the mass of the sample. In Fig. 3a we have plotted the evolution for two different sample masses (4.1 and 6.2 mg). The evolution is smooth for the 4.1 mg sample, while an abrupt TG evolution accompanied by a sharp DSC peak is observed for the higher mass.

In oxygen, the decomposition consists of an exothermic oxidative reaction involving the formation of acetaldehyde and water as volatiles [12]:

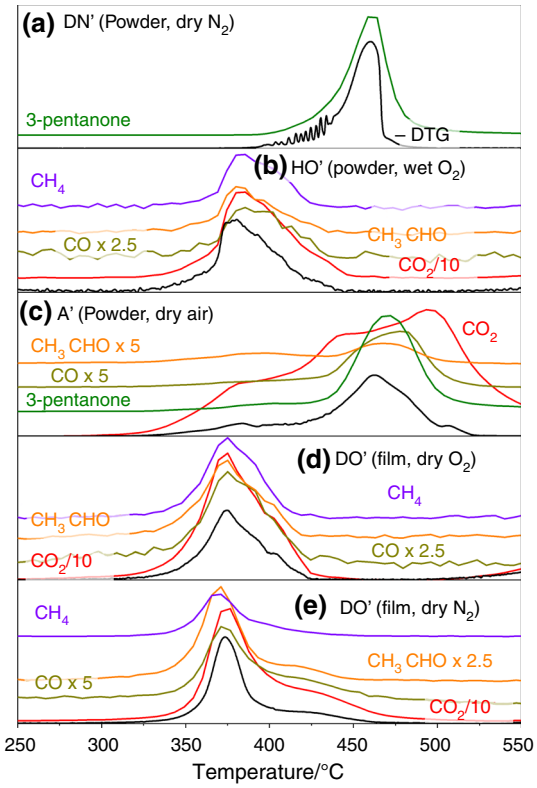

Fig. 4 TG-FTIR/EGA curves measured simultaneously during CaProp decomposition at 10 °C min^{-1} for powders and films under different atmospheres. The evolution of the volatiles is determined from the absorbance at the following characteristic frequencies: 1730 cm^{-1} (C = O) for propionic acid, 2356 cm^{-1} for CO_2, 2116 cm^{-1} for CO, 2750 cm^{-1} (CH) for acetaldehyde, 3017 cm^{-1} for methane and 3903 cm^{-1} for water

$$Ca\left(C_2H_5CO_2\right)_2 + 3/2O_2 \rightarrow 2CH_3CHO + H_2O + CaC_2O_4. \quad (6)$$

This reaction involves the formation of calcium oxalate as an intermediate product. Between 250 and 370 °C calcium oxalate decomposes at a very low rate according to [33]:

$$CaC_2O_4 \rightarrow 1/2CO_2 + 1/2C + CaCO_3, \quad (7)$$

and between 370 and 500 °C takes place the main decomposition stage:

$$CaC_2O_4 \rightarrow CO + CaCO_3. \quad (8)$$

Therefore, since calcium oxalate is not a stable intermediate, the decompositions of CaProp and calcium oxalate overlap. In addition, acetaldehyde decomposes to form methane and carbon monoxide:

$$CH_3CHO \rightarrow CH_4 + CO. \quad (9)$$

Despite the formation of CO and C during the decomposition of CaProp, the presence of O_2 prevents the formation of

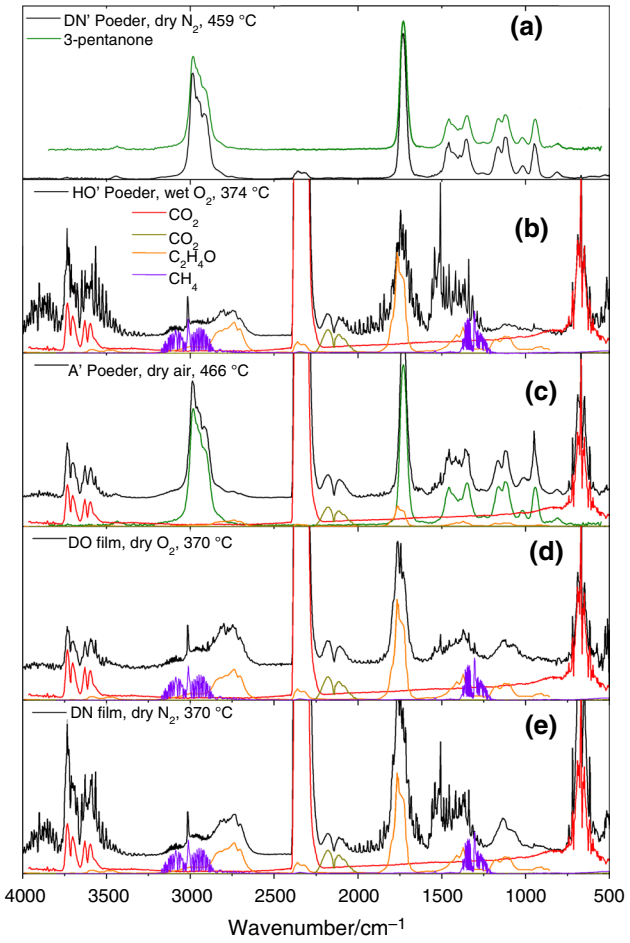

Fig. 5 FTIR spectra of the evolved gases at the peak temperatures of the decomposition evolutions shown in Fig. 4. The reference FTIR spectra have been obtained from [29]

carbon. Consequently, at 500 °C a white powder is obtained. The EA analysis (Table 1) confirms the complete removal of hydrogen and the amount of carbon is in perfect agreement with that of $CaCO_3$. In addition, XRD and IR analyses (not shown) confirm that the solid phase at 500 °C is calcite. Thus, CO_2 is formed from the oxidation of C and CO.

Comparison of the EGA-FTIR spectra (Fig. 5b) with the reference spectra of [29] leads to the identification of all expected volatiles related to the reaction of CaProp with oxygen (reactions 6–9): CO_2, CO, acetaldehyde, methane and water. Moreover, the evolution of these volatiles coincides with that of the mass loss rate (Fig. 4b). Note that in Fig. 4b the CO_2 signal is divided by a factor 10, i.e., CO_2 is clearly the main volatile released during the oxidative reaction.

The decomposition of CaProp in dry or wet O_2 is almost complete before the onset of radical decomposition, so these two mechanisms do not compete. However, in air, the lower amount of O_2 slows down the reactive pathway, thus favoring the onset of the radical pathway.

From Fig. 3, it can be seen that, as in O_2, in air the decomposition starts at 310 °C, the process is exothermic and the peak temperature of the DSC signal is also at 374 °C, but the evolved mass and the intensity of the DSC signal are much lower than in the O_2 atmosphere, which means that only a small amount of CaProp has been decomposed. Afterwards, CaProp melting is revealed by the weak endothermic DSC peak at the melting point (385 °C). In the melted CaProp, the oxygen diffusion is higher, thus increasing the mass loss rate and the DSC signal. However, after melting, both the reactive and radical pathways compete. The sharp decrease in the DSC signal around the DTG peak temperature, 466 °C, makes it clear that the radical pathway is the main decomposition mechanism in air. The FTIR spectrum at 466 °C (Fig. 5c) shows that the main volatiles are 3-pentanone and CO_2. The weak signal intensity related to acetaldehyde confirms that the main reaction pathway is the radical.

Film decomposition

As we have seen in Sect. 3.2, after dehydration or loss of propionic acid, the same phase is obtained in the films and in the powders: anhydrous CaProp. Therefore, the same mechanisms discussed in the previous section can be expected to explain the decomposition of the films. However, due to the different morphology, the decomposition kinetics may be different.

In O_2, the decomposition kinetics of films is quite similar to that of the powder (Fig. 3). The only difference is that the decomposition is slightly shifted at lower temperatures, about 5 °C. This is because the diffusion of O_2 is faster in the films due to the higher surface/volume ratio. However, this effect is small due to the high porosity and fine structure of the powders, as revealed by SEM (Fig. 1).

As for volatiles, from Fig. 5b and Fig. 5d we can observe that the same volatiles are formed in powders and films in O_2 and that their EGA peak shape is similar. Thus, the thermal decomposition of the films in O_2 is governed by the same mechanism that acts in the powder, the reactive oxidation of CaProp (Reactions 6–9).

The decomposition of the film in N_2 is very different from that of the powder. Surprisingly, from Fig. 5d and Fig. 5e we realize that the volatiles and film decomposition kinetics is the same in O_2 as in N_2. The only difference is that in O_2 a single DTG peak is observed, while in N_2 a second weak DTG peak appears around 420 °C. Therefore, in N_2 the main decomposition pathway of the films is oxidative degradation, and the radical mechanism, observed above 400 °C, only affects a minor amount of CaProp. This oxidation is due to

the presence of residual oxygen in the nominally oxygen-free atmosphere. In fact, it has already been shown that the films are very sensitive to residual oxygen, and that it is very difficult to create a totally inert atmosphere in films [13, 14, 16]. The effect of residual oxygen has been confirmed by varying the nitrogen flux in the TG: when the nitrogen flux is increased, the radical decomposition becomes more important, the amount of CO_2 is lower and more 3-pentanone is formed.

Whether the radical or oxidative mechanism dominates decomposition does not depend solely on the oxygen partial pressure. Indeed, in powders with circulating air, the radical pathway is the main decomposition mechanism whereas, in films and with a nominally inert atmosphere, the oxidative mechanism is the main one. In "inert atmosphere", oxidative decomposition dominates even though the oxygen partial pressure is lower than that of air. The higher surface/volume ratio of the films, plus the porosity of the films, greatly favors oxygen diffusion, whereas in powders intra-particle diffusion hinders the oxidative pathway in favor of the radical mechanism.

Finally, the kinetics and volatiles evolved in the films and powder are not affected by the presence of water vapor in the carrier gas. As in the decomposition of barium propionate [12], the difficulty in breaking the CaO−C(=O)R bond, which would yield the oxide, results in the formation of the oxalate or carbonate. Since hydrolysis involves the formation of the oxide, a humid atmosphere does not affect the decomposition of CaProp.

Thermal runaway

In exothermic reactions, thermal runaway (or combustion) occurs when the heat evolved from the reaction cannot be dissipated fast enough. Above a critical sample size, the reaction becomes locally unstable; it reaches a high-temperature state and the reaction accelerates greatly. In this state, the reaction can be considered adiabatic, since virtually all of the heat released by the reaction contributes to heating the sample [34]. Hence, for a sample to undergo thermal runaway, two conditions must be met: low heat dissipation and high enthalpy of reaction.

Powders are known to have a very low thermal conductivity, similar to that of the surrounding gas [35, 36], and propionate decomposition is usually a highly exothermic process with enthalpies around 10^6 J kg^{-1}, so they can easily undergo thermal runaway even for sample masses as low as those used in thermal analysis [13]. In the case of a thermal runaway, the TG curve shows a very abrupt mass loss and the DSC curve exhibits a very sharp exothermic peak [14, 37–39]. These two features can be identified in Fig. 3 for the 6.2 mg powder sample in O_2: a sudden drop in mass and a very sharp DSC peak that is off-scale are observed in Fig. 3b (the DSC signal at the peak is 133 mW mg^{-1}).

The critical mass (m_{cr}) for which combustion would occur in the case of powders inside a cylindrical crucible heated at a constant rate is given by [40, 41]:

$$m_{cr} = \rho\pi R^3 \sqrt{0.878\left(\frac{\gamma R^2}{5a} - 2\right)^{-1}}, \tag{10}$$

where ρ is the bulk density of powders, R is the radius of the crucible (3,45 mm for the 350 µL crucible), $a \equiv \lambda/\rho c$ is the thermal diffusivity, c is the specific heat capacity, λ is the thermal conductivity and

$$\gamma = A\theta_T(1+2\varepsilon)\left\{1-(2+\varepsilon+30\varepsilon^2)\frac{2}{\theta_T}\right\}e^{-1/\varepsilon},$$

$$\theta_T = \frac{E_A}{R_G T_{Kis}^2}\frac{q}{c}, \varepsilon = \frac{R_G T_{Kis}}{E_A},$$

and T_{Kis} is the temperature at which the reaction rate is at its maximum, and can be calculated from the Kissinger equation [42, 43].

The physical parameters used to determine the critical mass are listed in Table 2. The thermal conductivity and specific heat capacity have been obtained from DSC experiments for the sample in powder form [44, 45]. A tin bead (melting point 232 °C) was used to determine the thermal conductivity. The enthalpy of reaction has been determined from the integration of the DSC signal, Fig. 3b, of the 6.2 mg powder sample heated at 10 °C min^{-1} in dry O_2. The bulk density was determined using a 350 µL crucible and filling it with powder in the same manner as we filled the crucibles in the TG/DSC experiments. The kinetic parameters E_A and A have been obtained from isoconversional analysis of powders in dry O_2, (see Fig. 6 in the appendix), and for $\alpha = 0.1$ since the thermal runaway begins at approximately this degree of transformation. From these kinetic parameters and for a heating rate of 10 °C min^{-1} we obtain $T_{Kis} = 389$ °C. Application of Eq. 10 results in a critical mass of 5.7 mg; i.e., a sample of mass greater than this value should undergo combustion. The TG experiments in Fig. 3 (curves **DO'**) agree with this prediction: combustion occurs at 6.2 mg but not at 4.1 mg.

Conclusions

The initial powders are a mixture of anhydrous and monohydrate CaProp, while dried films crystallize in a new phase due to the presence of coordinated propionic acid. After dehydration and removal of the propionic acid, the same phase is obtained in films and powders: anhydrous CaProp.

Table 2 Physical parameters of CaProp

Specific heat capacity (c)/J kg^{-1} K^{-1}	1280 (260 °C)
Activation energy (E_A)/kJ mol^{-1}	227
Pre-exponential constant (A)/s^{-1}	8.45×10^{15}
Enthalpy of reaction (q)/J kg^{-1}	8.3×10^{6}
Bulk density/kg m^{-3}	488
Thermal conductivity (λ)/W m^{-1} K^{-1}	0.06 (232 °C)

During thermal decomposition of CaProp, two pathways compete: radical and reactive. The former involves the formation of 3-pentanone as a volatile, while the latter involves the formation of CO_2, CO, acetaldehyde, methane and water. Both pathways end with the formation of calcite. The reactive pathway is highly exothermic as it involves the reaction of oxygen with CaProp and dominates at low temperatures. In contrast, the enthalpy of the radical pathway is much lower, occurring at higher temperatures.

Powder follows the reactive path in O_2. Decomposition starts at low temperatures (about 310 °C). In inert atmosphere, decomposition starts near the melting point of CaProp (385 °C) and follows the radical pathway. Melting does not affect the kinetics of the radical pathway, but since gas diffusion in the liquid is higher, it significantly accelerates the oxidative pathway. However, this acceleration only occurs for heating rates high enough to shift the decomposition onset near the melting point.

In inert atmosphere, the product contains residual carbon while no residual carbon is observed in O_2. In air, both mechanisms compete, the oxidative pathway initiates decomposition, but at higher temperature the radical pathway becomes the main decomposition mechanism.

The decomposition of films starts with the oxidative pathway, either in O_2 or in a nominally inert atmosphere. In "inert atmosphere" the two pathways compete because of the great sensitivity of the films to the presence of residual oxygen: the more inert the atmosphere, the more important the radical pathway. Whether the reaction is dominated by the oxidative pathway or not depends on the actual oxygen partial pressure, the surface-to-volume ratio and the porosity of the sample. The oxidative pathway in "inert atmosphere" is favored by a faster diffusion of O_2 trough the sample and a large free surface area.

Finally, CaProp powders can easily undergo thermal runaway in oxygen due to their low thermal conductivity and high enthalpy of reaction.

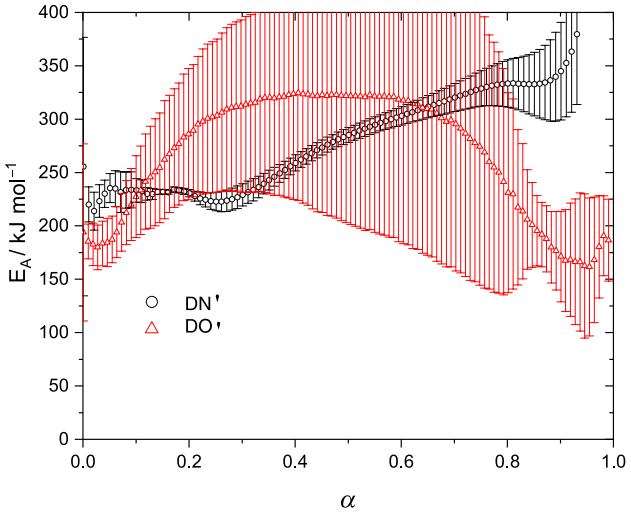

Fig. 6 Apparent activation energy obtained from exact Ortega analysis for TG experiments performed in dry O_2 (triangles) and dry N_2 (circumferences). Bars are provided to indicate the uncertainty in the apparent activation energy

Appendix: Kinetic analysis

The thermal decomposition of organometallic compounds is typically a thermally activated process. As a first approximation, when the kinetics is governed by a single step, it can be described by [46]:

$$\frac{d\alpha}{dt} = A e^{-\frac{E_A}{R_G T}} f(\alpha), \tag{11}$$

where T is the temperature, α is the degree of transformation ($0 \leq \alpha \leq 1$), E_A and A are the activation energy and the pre-exponential constant, respectively, and R_G is the universal gas constant.

To deal with more complex transformations, isoconversional methods are based on the more general isoconversional principle which assumes that, at a given degree of transformation, the transformation rate depends only on the temperature and the degree of transformation [47–49]:

$$\left[\frac{d\ln(d\alpha/dt)}{dT^{-1}}\right]_\alpha = -\frac{E_\alpha}{R_G}, \tag{12}$$

where E_α is the apparent activation energy at a particular α.

To determine the kinetic parameters of the oxidative and radical pathways, we performed TG experiments on dry O_2 and dry N_2, respectively. For each analysis we performed 5 experiments at different heating rates (2.5, 5, 10, 20 and 30 °C min^{-1}). These two kinetic analyses cover the temperature range from 300 to 530 °C. The curves were analyzed by the exact isoconversional method of Ortega [50, 51]. In the case of experiments performed in dry O_2, samples of mass less than 2 mg were used to avoid local overheating (see

Sect. 3.5). The apparent activation energy obtained from the kinetic analysis is shown in Fig. 6. The non-constancy of the apparent activation energy reveals that the decomposition in O_2 and N_2 is a complex process.

As expected, the result of the isoconversional analysis in N_2 differs significantly from the one obtained in O_2, since, as we have seen, the decomposition mechanism is different in N_2 than in O_2. However, the most relevant feature is the large statistical error related to the determination of the apparent activation energy in O_2. The reason is that for $\alpha > 0.1$, the CaProp melting overlaps with its thermal decomposition. Melting is a first-order phase transition; the melting temperature is independent of the heating rate. Therefore, isoconversional analysis results in abnormally high values of the activation energy, i.e., isoconversional analysis does not provide a reliable kinetic analysis for $\alpha > 0.1$. The overlap of melting with decomposition may be the reason for the large fluctuations of the activation energy reported by [24].

Acknowledgements This work was funded by Spanish Ministry of Science, Innovation and Universities REBCOTLAG project (PID2021-127297OB-C22, co-financed by the European Regional Development Fund, MCIU/AEI/FEDER, UE) and by the Catalan Government, Generalitat of Catalunya, (2017-SGR-1519). Daniel Sanchez-Rodriguez acknowledges the support received from the Beatriu de Pinós Programme and the Ministry of Research and Universities of the Government of Catalonia (Fellowship BP00069). Authors thank the Scientific Services at UdG.

Author Contributions Data collection and analysis were performed by Zaidi Sihem and Daniel Sanchez-Rodriguez. Experiment design and planning were performed by Jordi Farjas and Daniel Sanchez-Rodriguez. Kinetic Analysis and calculations were performed by Jordi Farjas and Daniel Sanchez-Rodriguez. Characterization of the physical parameters for thermal runaway were done by Zaidi Sihem and Pere Roura-Grabulosa. Jordi Farjas wrote the manuscript. Scientific discussion and mansucript revision by Pere Roura-Grabulosa and Mohamed Dammak.

Funding Open Access funding provided thanks to the CRUE-CSIC agreement with Springer Nature.

Declarations

Conflict of interest There are no conflicts of interest to declare.

References

1. Lück JM. Antimicrobial food additives, vol. 2. Berlin: Springer; 1997. p. 262. https://doi.org/10.1007/978-3-642-59202-7.
2. Frazier WCWC, Westhoff DC. Food microbiology. 4th ed. New York: McGraw-Hill; 1988. p. 539.
3. Zhang F, Nan X, Wang H, Guo Y, Xiong B. Research on the applications of calcium propionate in dairy cows: a review. Animals. 2020;10(8):1–13. https://doi.org/10.3390/ani10081336.
4. Sequeira S, Phillips A, Cabrita E, Macedo M. Antifungal treatment of paper with calcium propionate and parabens: short-term and long-term effects. Int Biodeterior Biodegr. 2017;120:203–15. https://doi.org/10.1016/j.ibiod.2017.03.005.
5. Betancur-Granados N, Molina JE, Pöllmann H, Tobón JI, Restrepo-Baena OJ. Influence of metallic precursors in the mineralogy and reactivity of belite cement clinkers obtained by flame spray pyrolysis. Mater Today Commun. 2021;26: 101917. https://doi.org/10.1016/j.mtcomm.2020.101917.
6. Patsias A, Nimmo W, Gibbs B, Williams P. Calcium-based sorbents for simultaneous NOx/SOx reduction in a down-fired furnace. Fuel. 2005;84(14–15):1864–73. https://doi.org/10.1016/j.fuel.2005.03.009.
7. Hites RA, Biemann K. Mechanism of ketonic decarboxylation. Pyrolysis of calcium decanoate. J Am Chem Soc. 1972;94(16):5772–7. https://doi.org/10.1021/ja00771a039.
8. Grivel JCC. Thermal decomposition of yttrium(III) propionate and butyrate. J Anal Appl Pyrolysis. 2013;101:185–92. https://doi.org/10.1016/j.jaap.2013.01.011.
9. Nasui M, Petrisor T, Mos R, Mesaros A, Varga R, Vasile B, Ristoiu T, Ciontea L, Petrisor T. Synthesis, crystal structure and thermal decomposition kinetics of yttrium propionate. J Anal Appl Pyrolysis. 2014;106:92–8. https://doi.org/10.1016/j.jaap.2014.01.004.
10. Grivel JC. Thermal decomposition of lutetium propionate. J Anal Appl Pyrolysis. 2010;89(2):250–4. https://doi.org/10.1016/j.jaap.2010.08.011.
11. Nasui M, Bogatan Pop C, Ciontea L, Petrisor T. Synthesis, crystal structure modeling. J Anal Appl Pyrolysis. 2012. https://doi.org/10.1016/j.jaap.2012.05.003.
12. Rasi S, Ricart S, Obradors X, Puig T, Roura-Grabulosa P, Farjas J. Radical and oxidative pathways in the pyrolysis of a barium propionate-acetate salt. J Anal Appl Pyrolysis. 2019;141:104–640. https://doi.org/10.1016/j.jaap.2019.104640.
13. Rasi S, Ricart S, Obradors X, Puig T, Roura P, Farjas J. Thermal decomposition of yttrium propionate: film and powder. J Anal Appl Pyrolysis. 2018;133:225–33. https://doi.org/10.1016/j.jaap.2018.03.021.
14. Roura P, Farjas J, Eloussifi H, Carreras L, Ricart S, Puig T, Obradors X. Thermal analysis of metal organic precursors for functional oxide preparation: thin films versus powders. Thermochim Acta. 2015;601:1–8. https://doi.org/10.1016/j.tca.2014.12.016.
15. Rasi S, Silveri F, Ricart S, Obradors X, Puig T, Roura-Grabulosa P, Farjas J. Thermal decomposition of CuProp2: In-situ analysis of film and powder pyrolysis. J Anal Appl Pyrolysis. 2019;140:312–20. https://doi.org/10.1016/j.jaap.2019.04.008.
16. Roura P, Farjas J, Ricart S, Aklalouch M, Guzman R, Arbiol J, Puig T, Calleja A, Peña-Rodríguez O, Garriga M, Obradors X. Synthesis of nanocrystalline ceria thin films by low-temperature thermal decomposition of Ce-propionate. Thin Solid Films. 2012;520(6):1949–53. https://doi.org/10.1016/j.tsf.2011.09.058.
17. Gobert-Ranchoux E, Charbonnier F. Comportement thermique des propionates hydrates de calcium, strontium et baryum. J Therm Anal. 1977;12(1):33–42. https://doi.org/10.1007/BF01909853.
18. O'Connell CA, Dollimore D. A study of the decomposition of calcium propionate, using simultaneous TG-DTA. Thermochim

Acta. 2000;357–358:79–87. https://doi.org/10.1016/S0040-6031(00)00371-3.
19. Valor A, Reguera E, Torres-García E, Mendoza S, Sanchez-Sinencio F. Thermal decomposition of the calcium salts of several carboxylic acids. Thermochim Acta. 2002;389(1–2):133–9. https://doi.org/10.1016/S0040-6031(02)00010-2.
20. Li T, Lorenz H, Seidel-Morgenstern A. Solubility study and thermal stability analysis of calcium propionate. Chem Eng Technol. 2017;40(7):1221–30. https://doi.org/10.1002/ceat.201600479.
21. Barnes PA, Stephenson G, Warrington SB. The use of TA - GLC - MS as a quantitative specific EGA technique for the investigation of complex thermal decomposition reactions: the thermal decomposition of calcium propanoate. J Therm Anal. 1982;25(2):299–311. https://doi.org/10.1007/BF01912955.
22. Nimmo W, Patsias AA, Hall WJ, Williams PT. Characterization of a process for the in-furnace reduction of NO x, SO 2, and HCl by carboxylic salts of calcium. Ind Eng Chem Res. 2005;44(12):4484–94. https://doi.org/10.1021/ie0501780.
23. Sanchez-Rodriguez D, Farjas J, Roura P, Ricart S, Mestres N, Obradors X, Puig T. Thermal analysis for low temperature synthesis of oxide thin films from chemical solutions. J Phys Chem C. 2013;117(39):20133–8. https://doi.org/10.1021/jp4049742.
24. Niu S, Han K, Lu C. Kinetic calculations for the thermal decomposition of calcium propionate under non-isothermal conditions. Chinese Sci Bull. 2011;56(12):1278–84. https://doi.org/10.1007/s11434-010-4065-8.
25. Cheda JAR, García MV, Redondo MI, Gargani S, Ferloni P. Short chain copper(II) n -alkanoate liquid crystals. Liq Cryst. 2004;31(1):1–14. https://doi.org/10.1080/02678290310001628500.
26. Zeleňák V, Vargová Z, Györyová K. Correlation of infrared spectra of zinc(II) carboxylates with their structures. Spectrochim Acta A Mol Biomol Spectrosc. 2007;66(2):262–72. https://doi.org/10.1016/j.saa.2006.02.050.
27. Deacon G. Relationships between the carbon-oxygen stretching frequencies of carboxylato complexes and the type of carboxylate coordination. Coord Chem Rev. 1980;33(3):227–50. https://doi.org/10.1016/S0010-8545(00)80455-5.
28. Kakihana M, Nagumo T. Assignment for the infrared spectrum of solid sodium propionate from low-temperature measurements in combination with 13C isotopic shifts. Zeitschrift für Naturforsch A. 1987;42(5):477–84. https://doi.org/10.1515/zna-1987-0509.
29. Wallace W. In: Linstrom P, Mallard W, editors. NIST Chem WebBook. Gaithersburg: NIST Stand Ref Database. Institute of Standards and Technology; 2019;20899. https://doi.org/10.18434/T4D303.
30. Farhadi Khouzani M, Chevrier DM, Güttlein P, Hauser K, Zhang P, Hedin N, Gebauer D. Disordered amorphous calcium carbonate from direct precipitation. CrystEngComm. 2015;17(26):4842–9. https://doi.org/10.1039/c5ce00720h.
31. Rodriguez-Blanco JD, Shaw S, Benning LG. The kinetics and mechanisms of amorphous calcium carbonate (ACC) crystallization to calcite, via vaterite. Nanoscale. 2011;3(1):265–71. https://doi.org/10.1039/c0nr00589d.
32. Verdonk A, Broersma A. Thermal decomposition of barium oxalate hemihydrate BaC2O4·0.5H2O. Thermochim Acta. 1973;6(1):95–110. https://doi.org/10.1016/0040-6031(73)80009-7.
33. Hourlier D. Thermal decomposition of calcium oxalate: beyond appearances. J Therm Anal Calorim. 2019;136(6):2221–9. https://doi.org/10.1007/s10973-018-7888-1.
34. Patil KC, Aruna S, Mimani T. Combustion synthesis: an update. Curr Opin Solid State Mater Sci. 2002;6(6):507–12. https://doi.org/10.1016/S1359-0286(02)00123-7.
35. Klemensiewicz Z. Thermal conductivity of powders. Nature. 1949;164(4170):589–589. https://doi.org/10.1038/164589b0.
36. Mukasyan AS, Rogachev AS. Discrete reaction waves: Gasless combustion of solid powder mixtures. Prog Energy Combust Sci. 2008;34(3):377–416. https://doi.org/10.1016/j.pecs.2007.09.002.
37. Boddington T, Hongtu F, Laye P, Nawaz M, Nelson DC. Thermal runaway by thermal analysis. Thermochimica Acta. 1990;170:81–7. https://doi.org/10.1016/0040-6031(90)80526-5.
38. Neeft JP, Hoornaert F, Makkee M, Moulijn JA. The effects of heat and mass transfer in thermogravimetrical analysis A case study towards the catalytic oxidation of soot. Thermochimica Acta. 1996;287(2):261–78. https://doi.org/10.1016/S0040-6031(96)03002-X.
39. Sánchez-Rodríguez D, Wada H, Yamaguchi S, Farjas J, Yahiro H. Self-propagating high-temperature synthesis of LaMO3 perovskite-type oxide using heteronuclearcyano metal complex precursors. J Alloys Compounds. 2015;649:1291–9. https://doi.org/10.1016/j.jallcom.2015.07.246.
40. Sánchez-Rodriguez D, Farjas J, Roura P. The critical conditions for thermal explosion in a system heated at a constant rate. Combust Flame. 2017;186:211–9. https://doi.org/10.1016/j.combustflame.2017.08.008.
41. Zghal I, Farjas J, Camps J, Sánchez-Rodríguez D, Dammak M, Roura-Grabulosa P. Use of thermal analysis to predict the conditions for thermal explosion to occur: application to a Ce triethanolamine complex. J Therm Anal Calorim. 2020. https://doi.org/10.1007/s10973-020-10262-4.
42. Kissinger HE. Reaction kinetics in differential thermal analysis. Anal Chem. 1957;29(11):1702–6. https://doi.org/10.1021/ac60131a045.
43. Farjas Silva J, Roura P. Exact analytical solution for the Kissinger equation: determination of the peak temperature and general properties of thermally activated transformations. Thermochimica Acta. 2014;598:51–8. https://doi.org/10.1016/j.tca.2014.10.024.
44. Pujula M, Sánchez-Rodríguez D, Lopez-Olmedo JP, Farjas J, Roura P. Measuring thermal conductivity of powders with differential scanning calorimetry. J Therm Anal Calorim. 2016;125(2):571–7. https://doi.org/10.1007/s10973-016-5274-4.
45. Sánchez-Rodríguez D, López-Olmedo JP, Farjas J, Roura P. Determination of thermal conductivity of powders in different atmospheres by differential scanning calorimetry. J Therm Anal Calorim. 2015;121:469–73. https://doi.org/10.1007/s10973-015-4429-z.
46. Šesták J. Thermophysical properties of solids, their measurements and theoretical analysis, vol. 12D. Amsterdam: Elsevier; 1984.
47. Vyazovkin S. Evaluation of activation energy of thermally stimulated solid-state reactions under arbitrary variation of temperature. J Comput Chem. 1997;18(3):393–402. https://doi.org/10.1002/(SICI)1096-987X(199702)18:3<393::AID-JCC9>3.0.CO;2-P.
48. Farjas J, Roura P. Isoconversional analysis of solid state transformations. A critical review. Part II. Complex transformations. J Therm Anal Calorim. 2011;105(3):767–73. https://doi.org/10.1007/s10973-011-1447-3.
49. Vyazovkin S, Burnham AK, Favergeon L, Koga N, Moukhina E, Pérez-Maqueda LA, Sbirrazzuoli N. ICTAC Kinetics Committee recommendations for analysis of multi-step kinetics. Thermochimica Acta. 2020. https://doi.org/10.1016/j.tca.2020.178597.
50. Ortega A. A simple and precise linear integral method for isoconversional data. Thermochimica Acta. 2008;474(1–2):81–6. https://doi.org/10.1016/j.tca.2008.05.003.

51. Farjas J, Roura P. Isoconversional analysis of solid state transformations. A critical review. Part I. Single step transformations with constant activation energy. J Therm Anal Calorim. 2011;105(3):757–66. https://doi.org/10.1007/s10973-011-1446-4.